Seismic imaging of a carbonate rock block with fracture-induced anisotropy

Rie Nakata (University of Tokyo), Christophe Matonti (Aix-Marseille Université, CEREGE), Nori Nakata (MIT), Yves Guglielmi (Lawrence Berkley National Laboratory), Sophie Viseur, (Aix-Marseille Université, CEREGE)

Summary

Seismic experiments on a meter-scale rock sample characterize spatial heterogeneities at outcrop scale, and potentially bridge the gap between laboratory experiments and conventional field seismic experiments. Using a real seismic dataset of a fractured carbonate rock sample, we demonstrate strong potentials of small rock-block experiments, and endeavor towards full waveform analyses, such as full waveform inversion. We were able to place sources and receivers to surround the sample and acquired the data to optimally illuminate internal structures along chosen 2D planes. The observed waveforms comprised clear but complicated P- and S-wave direct arrivals and free surface reflections from all sides of the block. Beamforming (slant-stacking) was capable of extracting hidden complex arrivals. By exploiting both P and S arrivals, we successfully estimated parameters of apparent tilted transverse anisotropy with a symmetry axis normal to the 10 cm-scale fractures. In order to delineate heterogeneities in the sample due to fractures, we proposed to apply full waveform inversion to the dataset. With synthetic studies, we illustrated that the velocity model can be nearly perfectly reconstructed at a half-wavelength scale.

Introduction

Seismic experiments on small rock samples of a meter scale can image their internal structures of the order of centimeters, and potentially act as if a CT scan of outcrops revealing detailed fracture and fault development. This scale is unique, potentially bridges the gap between laboratory-scale experiments and field-scale surface seismic surveys, and sheds lights into apparent and actual properties (e.g. apparent anisotropy and fracture distributions). We can design acquisitions to surround a rock sample, characterize 3D heterogeneities and eliminate imaging and inversion biases arising from suboptimal subsurface illumination.

We explore potentials and challenges of seismic analysis of meter-scale samples by using real data sets acquired for a limestone block (Figure 1a) that contains a multi-set of fractures with various degrees of diagenesis (Matonti et al., 2017). We observe that the seismic record is much richer than just first-arrival traveltime-picks of a particular phase. These waveforms are essential to achieve high resolution, and we aim to ultimately employ full waveform analysis such as full waveform inversion (e.g., Kamei et al., 2012, Forghani-Arani et al., 2017) and reverse-time migration (e.g. Nakata and Shelly, 2019). We conduct detailed investigations into understanding complex phases in the data and demonstrate advantages of using various phases by combining P and S waves. At last, we demonstrate how full waveform inversion can potentially estimate fine-scale structures by exploiting later reflected and diffracted arrivals.

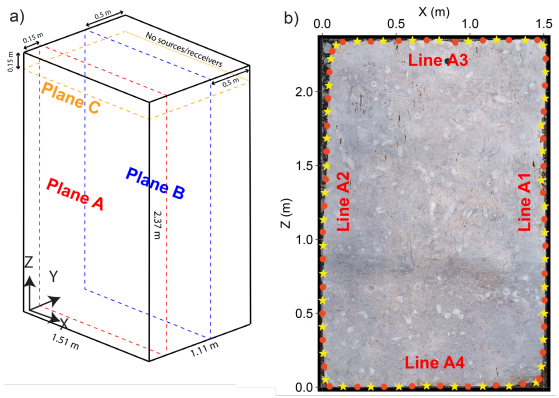

Figure 1 (a) Schematic diagram of a carbonate rock block used for the experiment. The red, blue and yellow dashed lines indicate acquisition planes. (b) Photo of a vertical surface of the rock near the red lines in (a). The yellow stars and red circles indicate the location of sources and receivers respectively. (modified from Matonti et al. 2017).

Experiment setup

Seismic experiments were conducted by using a limestone block with a size of 2.37 m x 1.51 m x 1.1 m (Figure 1a). The rock is characterized by a very low porosity (< 1.5 %), and a well-developed network of fractures (Figure 1b). Three 2D seismic data acquisitions were conducted to characterize Planes A-C by placing sources and receivers at the surface of the rock along red, yellow, and blue dashed lines (Figure 1a). The acquisition design enables us to obtain a tomographic information of planes A-C, and as we see later delineate discontinuities in a plane normal to them.

In this study, we focus on a seismic dataset acquired in Plane A, and denote the survey lines as Line A1, A2, A3 and A4 (Figure 1b). Sources and receivers were located at approximately 18 cm intervals. Piezoelectric transducers were used as both sources and receivers, and a receiver array consisted of 4 sensors. The sources were designed to excite

Seismic imaging of a carbonate rock block with fracture-induced anisotropy

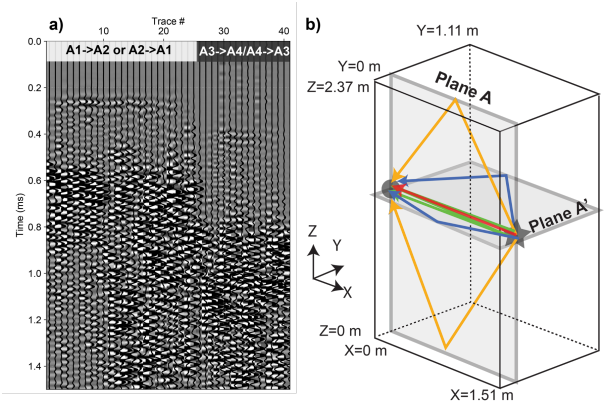

Figure 2 (a) Amplitude-normalized same-level gather after application of 5-40 kHz bandpass filter. (b) Schematic diagrams of 3D ray paths of for a source-receiver pair at the same Z (A1 → A2). The solid lines indicate (red) direct, (yellow) reflected waves from the XY surfaces, (green) a multiple of red reflected from the YZ surfaces, and (blue) the reflected wave from the XZ surfaces (plane A').

P-wave energy at a peak frequency of 55 kHz. The sampling rate is 1 MHz.

Waveform analysis

The observed seismic record shows reasonably good signal-to-noise ratios. The data contain frequency contents between 5 and 120 kHz, with several frequency notches. In Figure 2, we display the "same-level" gather (in a similar manner to cross-well survey data); a collection of traces where a source and a receiver are located along A1 or A2 at the opposite side of the rock block but at the same Z, or along A3 or A4 at same X. Note that we apply a lowpass filter at 40 kHz, since strong reverberation was present at 45 kHz. We expect to observe direct P- and S-wave transmissions, scattered waves, and their free surface reflections from all sides of the block (Figure 3).

P-wave first arrivals are clear and show mild perturbations between traces indicating some velocity perturbation within Plane A. P waves apparently propagates faster in the Z direction than in the X direction, suggesting the existence of anisotropy. After direct P, weak scattered waves are present. In addition to usual free-surface multiples from the YZ surfaces (green in Figure 2b), we observe free-surface reflections from the XY surfaces (yellow), and from the XZ surfaces (blue). Some of these arrivals are more evident in shot or receiver gathers.

We observe strong arrivals approximately at 0.6 ms for A1-A2 pairs, and 0.8 ms for A3-A4 pairs, which are either S-wave or surface waves. Surface waves may be excited at the XZ surface at Y=0 due to the proximity to the source. However, the waveforms do not show velocity dispersion, and thus we consider the wave packet as S-wave arrivals.

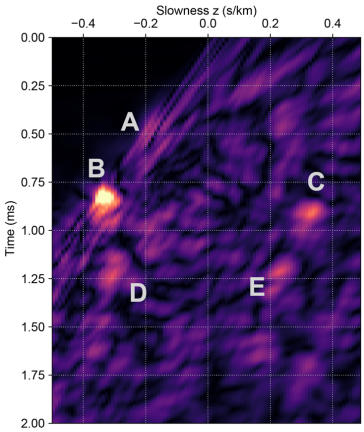

Figure 3: Beamformed intensity of a shot gather recorded by receivers along the line A1 (x=1.51 m) for a source at a top-right corner of the rock sample. We use the furthest receiver from the source as the reference. A indicates the direct P wave energy, B the direct S wave energy, and C the S reflection for the other side of the wall. D and E may be SS multiples.

Beamforming

We confirmed that the data contain S-waves, but further analysis is required before utilizing these S-waveforms to identify their wave types (i.e. direct/converted/reflected), as sources were supposed to excite P-energy dominantly. Beamforming (i.e., slant stacking) is a powerful tool to estimate wave velocities, propagation directions, intensity, and hence wave types (Rost and Stein, 2002, Nakata et al., 2016). We apply the beamforming to the shot gather of the source at the top-right corner recorded by receivers along the line A1. Here we take beamformed wavefields as

$$\boldsymbol{d}(\boldsymbol{p},\boldsymbol{t}) = \sum_r \boldsymbol{u}(\boldsymbol{r},\boldsymbol{t}-\boldsymbol{\tau}(\boldsymbol{r},\boldsymbol{p})),$$

where $\boldsymbol{r}$ is the receiver, $\boldsymbol{p}$ is apparent slowness along the receiver line, $\boldsymbol{d}(\boldsymbol{p},\boldsymbol{t})$ is the beamformed wavefields at specific slowness, $\boldsymbol{u}(\boldsymbol{r},\boldsymbol{t})$ is the observed waveforms at receivers, $\boldsymbol{\tau}(\boldsymbol{r},\boldsymbol{p})$ is the relative time shift from the reference point. First, we apply a bandpass filter between 5-20 kHz to avoid spatial aliasing and improve stacking power for better signal-to-noise ratio. Then we scan slownesses from -0.5 – 0.5 s/km, where the negative slowness indicates the wave from the source to receivers and the positive toward the source. After beamforming, we compute the envelope of the wavefields to interpret the wave intensity.

The most energetic wave (Figure 4 highlighted by B) propagates from the source at the velocity of 2.86 km/s. Combined with the arrival time of 0.8 s, we consider Wave B as the direct S wave, suggesting the source has excited both P- and S-wave energy. Wave C is the SS reflected wave from the surface, as slowness of Wave C is the same absolute value as Wave B, but in opposite sign. Waves D and E have a slightly larger apparent propagation velocities than Wave

B (direct S), and larger energy than Wave A (direct P). We interpret Waves D and E as SS reflected waves from the surfaces of the block, since their incident angle computed from their slowness and S-wave velocity is 30-45 degrees. With the knowledge of P wave velocity being approximately 5-6 km, Wave A is the direct P wave propagated at 5 km/s.

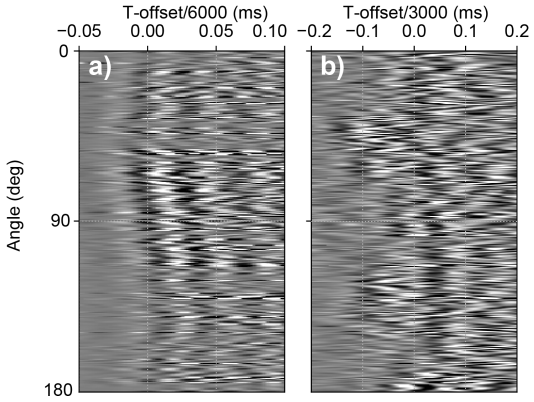

Figure 4: Deconvolved observed data sorted with respect to an angle between each source-receiver pair. We apply linear moveout using (a) 6000 m/s, and (b) 3000 m/s to illustrate angle dependence of (a) P- and (b) S-wave arrivals.

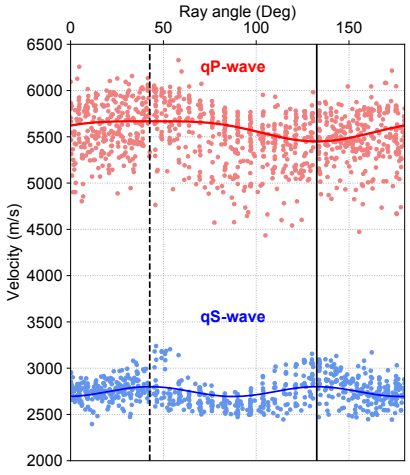

Figure 5: Picked (red) P- and (blue) S-wave velocities in dots, along with estimated (red) P- and (blue) S-wave velocity values obtained from the best fitted anisotropic TTI model in solid lines. The solid and dashed lines indicate the symmetry axis and its normal direction.

Anisotropy

Since the direct P- and S-wave arrivals were confirmed in the data, we estimate Thomsen parameters (Thomsen 1986). We display the observed waveforms sorted by a source-receiver aperture angle in Figure 4, after applying the linear moveout with respect to 6000 m/s (Figure 4a) and 3000 m/s (Figure 4b). The observed data are deconvolved to remove oscillations in a source wavelet. Both P-wave and S-wave arrivals are clearly angle-dependent, but two waves become fastest at different angles. P-wave become fastest at one specific angle, but S-wave is fastest at two different angles, as seen in transverse isotropic media (Tsvankin, 2012).

We automatically pick P and S first arrivals, remove outliers, and calculate (phase) velocities of P and S waves (v_p^{obs}, v_s^{obs}) by assuming a straight ray (Figure 5). The P- and S-wave velocities clearly have a strong angle dependence with a maximum of +/- 500 m/s for P-waves, and +/- 300 m/s for S-waves. Next, we assume tilted transverse isotropy (TTI), and describe P and S waves by

$$v_p = v_{p0}(1 + \delta \sin^2\theta \cos^2\theta + \epsilon \sin^4\theta\ ),$$

$$v_s = v_{s0}\left(1 + \left(\frac{v_{p0}}{v_{s0}}\right)^2\ (\epsilon - \delta)\sin^2\theta \cos^2\theta\ \right).$$

where δ and ϵ is the Thomsen parameters, θ is the angle between a symmetry axis and a raypath, v_{p0} and v_{s0} are the P- and S-wave velocities at the symmetry axis, respectively. We perform a grid search over v_{p0}, v_{s0}, ϵ, δ and an angle of the symmetry axis, θ_0, and minimize an objective function,

$$E = \sum\left|v_p\ (v_{p0}, \delta, \epsilon, \theta_0) - v_p^{obs}\right| + \sum\left|v_s(v_{po}, v_{s0}, \delta, \epsilon, \theta_0) - v_s^{obs}\right|.$$

The topography of the sampled objective function (not shown) is close to convex and the inversion is thus robust, because of very good ray coverages and availability of both P- and S-wave information. Our final estimates are v_{p0} = 5450 m/s, v_{s0} = 2800 m/s, ϵ = 0.04, δ =0.08 and θ_0 =-48 deg, The predicted v_p and v_s from the best fitted anisotropic parameters reproduce the overall trend of the observed values, confirming the validity of the estimated anisotropic parameters and the TTI assumption (Figure 5). The anisotropy is fracture induced, since the symmetry axis is perpendicular to the sealed fractures of 44-degree strike identified from careful visual examination by Matonti et al. (2017). Remaining perturbation in velocities suggest that velocity and anisotropy structures of the rock are heterogeneous as seen in Figure 2a, and that more sophisticated analysis will reveal their spatial variations.

Seismic imaging of a carbonate rock block with fracture-induced anisotropy

Towards full waveform inversion

Full waveform inversion estimates fine-scale spatial distribution of subsurface anisotropic elastic parameters by fully utilizing waveform information (Tarantola 1984; Afanasiev et al. 2013; Kamei et al. 2017). The full waveform inversion methods delineate the structures at a half-wavelength scale (Wu and Toksoz, 1989), but suffer from severe non-uniqueness due to nonlinearity and ill-conditioning. Since estimating anisotropy parameters is very ill-conditioned (Prieux et al. 2004), we intend to update only velocity parameters. Before actually applying full waveform inversion to the field block data, we examine their performance using synthetic data. As we have not identified strong converted waves, we can perform full waveform inversion separately for P- and S-waves at least as a first step.

Thus, in this study, we focus on P-waves and use frequency-domain anisotropic acoustic full waveform inversion with absorbing boundary conditions (Pratt et al. 2004; Afanasiev et al. 2014). The following discussions can be expanded for S-waves. To evaluate spatial resolution, we create a randomly heterogeneous model with velocity perturbations of ~ +/- 500 m/s (as in Figure 5) that isotropically covers the wavenumber domain (Figure 6). We start the inversion from a homogeneous model and update the velocity model using a frequency range from 6 kHz to 60 kHz. Our ideal source-receiver geometry allows us to retrieve the velocity structures without any horizontal or vertical biases and spatial aliasing effects as depicted in the estimated wavenumber spectra. Full waveform inversion nearly perfectly recovers velocity features as small as a half wavelength of the medium, i.e., our expected resolution. Hence, if we use up to 40 kHz, the spatial resolution of P-waves will be at ~6.25 cm regardless of directions of structures. As the fractures are, though narrow, mostly > 10 cm lengths (Matonti et al. 2017), we may be able to detect waves scattered at the fractures and infer properties. We may also increase the spatial resolution further if free-surface multiples are incorporated at the cost of 3D computation.

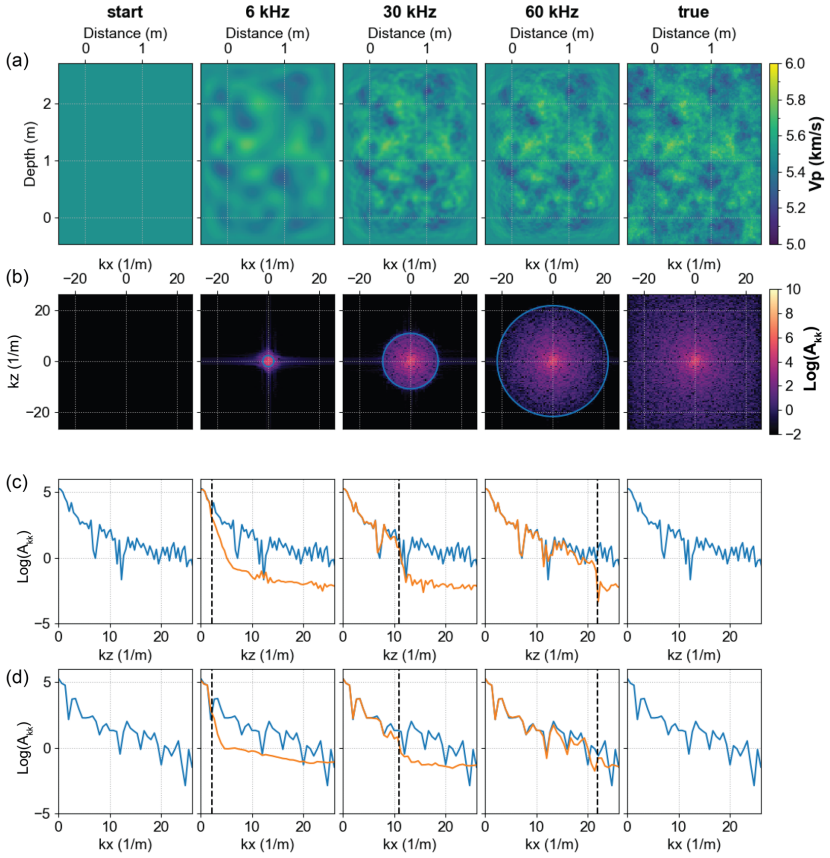

Figure 6: Full waveform inversion on block data. (a) Starting, estimated (6 kHz, 30 kHz, 60 kHz), and true P-wave velocity models. (b) Wavenumber spectra (A_{kk}) of (a) with a circle indicating the expected resolution (i.e., an average half wavelength of the medium). (c-d) (b) at (c) k_x=0, and (d) k_z=0 (1/m). Blue lines indicate the spectra of the true model, yellow liens the estimated models, and black dashed lines the expected resolution.

Conclusion

We carefully analyze seismic waveforms obtained from a carbonate-rock-block sample with a network of fractures. The presence of strong P- and S-wave first arrivals is critical to reliably estimate Thomson's anisotropic parameters in a TTI medium. Coherent S-wave signatures hidden in complex waveform data are extracted by beamforming techniques. Using synthetic data, we demonstrate that full waveform inversion can be a powerful tool to obtain high-resolution velocity models at a scale similar to fracture lengths. Our acquisition design is optimal and minimizes the biases in illumination. We are currently applying full waveform inversion to the real data and extending our approach to include full elastic and free-surface multiples.